Vacancy-type defects and oxygen incorporation in NiAl for advanced interconnects probed by monoenergetic positron beams and atom probe tomography

Akira Uedono[1,*], Claudia Fleischmann[2,3], Jean-Philippe Soulie[2], Mustafa Ayyad[2], Jeroen E. Scheerder[2], Christoph Adelmann[2], Jun Uzuhashi[4], Tadakatsu Ohkubo[4], Koji Michishio[5], Nagayasu Oshima[5], and Shoji Ishibashi[6]

[1]*Faculty of Pure and Applied Science, University of Tsukuba, Tsukuba, Ibaraki 305-8573, Japan*
[2]*Imec, Kapeldreef 75, 3001, Leuven, Belgium*
[3]*Quantum Solid-State Physics Group, KU Leuven, Celestijnenlaan 200D, 3001 Leuven, Belgium*
[4]*National Institute for Materials Science, Tsukuba 305-0047, Japan*
[5]*Research Institute for Measurement and Analytical Instrumentation (RIMA), National Institute of Advanced Industrial Science and Technology (AIST), Tsukuba, Ibaraki 305-8568, Japan*
[6]*Research Center for Computational Design of Advanced Functional Materials (CD-FMat), National Institute of Advanced Industrial Science and Technology (AIST), Tsukuba, Ibaraki 305-8568, Japan*

Abstract

Positron annihilation and atom probe tomography were used to study vacancy-type defects and their interaction with oxygen in 100-nm thick Ni_xAl_{1-x} deposited on a SiO_2/Si substrate. For as-deposited $Ni_{0.50}Al_{0.50}$, (i) monovacancy (V) and divacancy-type defects and (ii) vacancy clusters were found to coexist, and the clusters were estimated to be larger than V_{10}. Although no large change in the size of these vacancies was observed after post-deposition annealing below 500°C, the concentration of vacancy clusters decreased as temperature increased. Upon annealing, oxygen diffused mainly through grain boundaries. The oxygen incorporation was enhanced in Ni_xAl_{1-x} with high Ni content. The consumption of Al by surface oxides under Ni-rich conditions introduced defect-rich regions, and as a result, oxygen incorporation was enhanced likely via vacancy-assisted diffusion. The incorporated oxygen tended to couple with vacancies and form vacancy-oxygen complexes that were stable at 800°C annealing.

KEYWORDS: *NiAl, Interconnect, Vacancy, Positron annihilation, Atom probe tomography*

*Corresponding author: uedono.akira.gb@u.tsukuba.ac.jp

1. Introduction

Combinations of Cu and low dielectric constant materials have been widely used as interconnects and their inter-level insulators since mid-1990s [1,2]. They were introduced as a replacement for Al/SiO_2 interconnects because the Cu/low-*k* system can reduce the resistance-capacitance (RC) delay. Cu interconnects also show superior properties against electromigration (EM) compared to Al-based metallization [3]. The atomic transport by EM can introduce voids and hillocks in interconnections, which results in an increase in line resistance and/or short circuits between adjacent connections. The high EM reliability of Cu has played an important role in device reliabilities and their scaling. However, a continuous downscaling of integrated circuits requires aggressively shrinking signal lines and trenches, and as a result, Cu interconnects are now a major obstacle to scaling and limit device performance.

Major causes of the resistivity of signal lines in modern devices include not only their bulk resistivities (ρ_0) but also electron scattering at interfaces between metals and insulators (or barrier layers) and grain boundaries. According to the electrical resistivity models including such phenomena [4–7], the line resistivity is proportional to $\rho_0 \times \lambda$ for a given fixed line dimension, where λ is the mean free path for electron-phonon scattering. By using the so-called $\rho_0 \times \lambda$ products as a useful figure of merit, the search for alternative interconnect metals has been researched extensively [8–13]. Among several replacement candidates, Co and Ru have been mainly investigated [14–19]. The electrical resistivity model, however, does not involve variations in the surface scattering and grain boundary reflection due to their physical and chemical properties such as interface roughness, grain structures, and impurity incorporations. Because they depend on deposition and post-deposition processes of the interconnects, detailed knowledge based on the characterization of metal interconnects and related materials is indispensable.

EM relates closely to the device reliability and performance. Because the migration energies of atoms tend to increase as the melting points of metals increase, metal interconnects with high melting points are expected to show high resistance against EM. In this context, NiAl has been proposed as an interconnect binary metal [20–25] because of its relatively low values of ρ_0 (9×10^{-8} Ωm) and high melting temperature (1638°C) [26–29]. Although NiAl is the first candidate of intermetallic binary compounds as alternative interconnects, it faces several challenges. Soulié *et al*. [22] reported that the resistivity significantly increased as the thickness of NiAl decreased, and this tendency was accelerated by post-deposition annealing. The origin of the increase in layer resistivity was attributed to the segregation of Al introduced by the surface oxidation and interactions with the underlying SiO_2 film. Because the standard enthalpy of formation of Al_2O_3 (–1675 kJ/mol) is larger than that of SiO_2 (–911

kJ/mol), oxygen of SiO_2 adjacent NiAl can be pulled out from SiO_2 and form Al oxides. It was reported that the deposition of capping layers on NiAl, such as thin Si and Al layers, was effective at suppressing surface oxidation and improving thermal stability [21–24].

Because NiAl is deposited under nonthermal equilibrium conditions on substrates, a large number of point defects (mainly vacancy-type defects) are present in as-deposited layers. Because of the limited thermal budget for the back-end-of-line (BEOL) process, the post-deposition annealing is usually performed at below 500°C. During this annealing process, vacancy-type defects may dissociate, aggregate, and interact with grain boundaries. They might also interact with oxygen incorporated into NiAl. Because such behaviors of vacancy-type defects might relate to the resistivity and reliability of interconnects [30], the detailed behaviors of vacancies during annealing process need to be known. Positron annihilation effectively characterizes vacancy-type defects in solid-state materials [31,32] and has been successfully used to detect vacancy-type defects and open spaces in electroplated Cu for interconnects [30,33–38]. In the present study, we used monoenergetic positron beams to characterize vacancy-type defects in Ni_xAl_{1-x} (x = 0.45, 0.50, and 0.55). Grain growth and impurity incorporation in Ni_xAl_{1-x} by annealing were also studied by using scanning transmission electron microscopy (STEM), energy-dispersive x-ray spectroscopy (EDS), and atom probe tomography (APT).

2. Experimental

2.1 Sample preparation and characterization using STEM and APT

The sample structure used in the present experiments was $Ni_xAl_{1-x}/SiO_2/Si$ (x = 0.45, 0.50, and 0.55). A 600-nm-thick thermal SiO_2 was grown on 300-nm Si(100) wafers. Then, 100-nm-thick Ni_xAl_{1-x} films were deposited by a physical vapor deposition (PVD) process using co-sputtering of Al and Ni targets at room temperature. Base pressure during sputtering was 7×10^{-2} Pa in Ar plasma. After the deposition, the samples were annealed up to 800°C in vacuum (5×10^{-4} Pa), where the annealing time was 20 min. The electrical properties and crystallinity of Ni_xAl_{1-x} prepared by similar deposition conditions are described elsewhere [22,23,25]. For these samples, the crystalline phase of Ni_xAl_{1-x} was characterized by grazing-incidence x-ray diffraction (GIXRD). GIXRD patterns showed that the crystalline phase of Ni_xAl_{1-x} films was an ordered B2 β-NiAl phase, and no variation of the crystalline phase was observed between before and after annealing up to 400°C [25].

The sample morphologies were characterized by an aberration-corrected STEM (FEI Titan G2 80-200). The samples were cut into a thin lamella for STEM measurements, or needle-shaped tips for APT using a focused ion beam with the standard lift-out technique (Helios G4UX Dual Beam). A high-angle annular dark-field (HAADF) STEM observation was used to obtain cross-sectional images of

the samples with a 200-keV-electron beam. Distributions of oxygen in the STEM images were obtained by EDS. Qualitative oxygen depth profiles were also measured by secondary ion mass spectrometry (SIMS) using a low 400 eV Cs^+ beam for optimized depth resolution (2-2.2 nm/decade). To avoid any mass interference high mass resolution conditions were used. Absolute quantification of the oxygen content is not possible due to lack of reference standards for NiAl allows. Three-dimensional composition maps were obtained by a local electrode atom probe (CAMECA LEAP 5000XS). The measurements were carried out with 355-nm-wavelength laser pulsing of 50 pJ at a repetition rate of 500 kHz and a base temperature of 30 K.

2.2 Positron annihilation (experiments and theoretical calculations)

Vacancy-type defects in Ni_xAl_{1-x} were detected by using positron annihilation spectroscopy. Details of this technique are described elsewhere [31,32]. The Doppler broadening spectra of the annihilation radiation were measured by Ge detectors as a function of the incident positron energy E by a monoenergetic positron beam line (direct current type). The measured spectra were characterized by the S parameter, which is defined as the fraction of annihilation events in the energy range between 510.22 and 511.78 keV. The depth distributions of S were obtained from an analysis of the relationship between S and E using a computer code, VEPFIT [39]. Lifetime spectra of positrons were measured at E = 4 keV by using a pulsed monoenergetic positron beamline [40], where the total count of the spectrum was 4×10^6 and a time resolution was 0.26 ns (full width at half maximum). The lifetime spectrum of positrons, $N(t)$, is given by $N(t) = \Sigma\, \lambda_i I_i \exp(-\lambda_i t)$, where λ_i and I_i are the annihilation rate and the relative intensity of the i-th annihilation mode, respectively ($\Sigma\, I_i = 1$). The lifetime of positron, τ_i, is given by $1/\lambda_i$. The measured spectra were analyzed by using a code RESOLUTION [41], and the values of τ_i and I_i were determined from fittings.

The Doppler broadening spectra and positron lifetimes for the annihilation of positrons in Al, Ni, and B2 β-$Ni_{0.5}Al_{0.5}$ were simulated by QMAS (Quantum MAterials Simulator) code [42] based on the projector augmented-wave (PAW) method [43] and a plane-wave basis set. The Perdew–Burke–Ernzerhof-type generalized gradient approximation [44] was used to express the electronic exchange-correlation interaction. Calculations were performed on supercells with the size of 3 × 3 × 3 for FCC (Al and Ni) or 4 × 4 × 4 for BCC (β-$Ni_{0.5}Al_{0.5}$). They contain 108 or 128 atoms, respectively, if there are no defects. The supercell dimensions of β-$Ni_{0.5}Al_{0.5}$, for example, are 1.1548 nm × 1.1548 nm × 1.1548 nm. For the cases containing defects, atomic positions were computationally optimized. For vacancies in Al and most of d-block metals, the presence of the trapped positron affects the vacancy structure, and hence the calculated positron lifetime values vary significantly depending on the

presence or absence of the positron effect [45,46]. If a positron is trapped at a defect, the two-component density functional theory (TCDFT) scheme [47,48] should be applied. The electron and positron states as well as the atomic arrangements were consistently calculated for such cases using the TCDFT. For delocalized positron states, the positron effect on the electronic structure and the atomic arrangements was ignored. Further details of the computational scheme for the positron state are described in Ref. [45].

3. Results and Discussion

3.1 Grain growth and oxygen incorporation in Ni_xAl_{1-x} by isochronal annealing

Figure 1 shows cross-sectional HAADF STEM images and oxygen distributions in the corresponding STEM images for Ni_xA_{1-x} (x = 0.45, 0.50, and 0.55) before and after annealing at 500°C. For the as-deposited samples [Fig. 1(a1), (b1), and (c1)], columnar grains were observed. In these images, black lines and stripes correspond to grain boundaries. No large difference was observed in grain structures for the samples with different Ni content. In EDS images for these samples [Fig. 1(a2), (b2), and (c2)], white regions correspond to regions with high oxygen concentration. It can be seen that the sample surfaces were oxidized before annealing. From the comparison between STEM and EDS images, it can be concluded that oxygen diffused into the samples mainly through grain boundaries. For $Ni_{0.45}A_{0.55}$ after annealing at 500°C [Fig. 1(d1) and (d2)], the grain growth started from the $Ni_{0.45}A_{0.55}/SiO_2$ interface. For the samples with higher Ni content, that was not the case.

Figure 2 shows cross-sectional distributions of Ni, Al, and oxygen in Ni_xAl_{1-x} (x = 0.45, 0.50, and 0.55) before and after annealing at 500°C. These distributions of atoms were obtained from 10-nm thick vertical and 20-nm thick horizontal slices from the center of the three-dimensional atom maps, respectively. Green, blue, and purple points represent Ni, Al, and oxygen, respectively. The bottom of the vertical slice corresponds to the SiO_2 layer. The observed stripe patterns in these maps represent fluctuations in the Ni/Al atom density, potentially originating from differences in the evaporation probability of ions inside grains (lower ion density) and at grain boundaries (higher ion density) [49]. Thus, the pattern structure can be associated with grains and grain boundaries. For $Ni_{0.45}A_{0.55}$ after annealing at 500°C, the grain size increased, which agrees with the image obtained by STEM [Fig. 1(d1)]. From Fig. 1 and 2, it can be seen that the grain growth tends to be suppressed as the Ni content increases. In all films the oxygen distribution was not homogeneous and seemed to partly correlate with the locations of grain boundaries. For $Ni_{0.55}Al_{0.45}$ after annealing, oxygen was not only distributed through grain boundaries but also spread over grains. Comparing to the samples with high Ni content, oxygen incorporation was suppressed for $Ni_{0.45}Al_{0.55}$.

Figure 3 shows depth distributions of oxygen in Ni_xAl_{1-x} before (a) and after annealing at 500°C (b) obtained using SIMS. For the as-deposited samples, the oxygen concentration decreases monotonically from the surface to the Ni_xAl_{1-x}/SiO_2 interface, suggesting oxygen diffusion from the surface. The oxygen concentration increased after annealing at 500°C, which can be associated with surface oxidation and oxygen inclusion. For $Ni_{0.45}Al_{0.55}$ before and after annealing, the oxygen concentrations were lower than those for the samples with higher Ni content, consistent with the APT and EDS data.

NiAl has been investigated for high-temperature structural and aerospace applications because it shows excellent oxidation and corrosion resistance due to a thin Al_2O_3 layer being formed on NiAl by oxidation [50,51]. A drawback of the oxide formation is the introduction of void and cavities below the oxide, which is mainly due to Al being consumed by oxides and inward diffusion of Ni [52–54]. The void formation is accelerated for NiAl with high Ni content because of the small diffusion constant of Al [53]. These oxidation mechanisms were studied for NiAl oxidized at high temperatures (≥ 1000°C). As discussed in the next section, Ni_xAl_{1-x} deposited on SiO_2/Si substrate contained high-concentration vacancy-type defects. Thus, vacancy-assisted diffusion is likely to enhance oxidation and related atomic reactions at relatively low temperatures. For Ni_xAl_{1-x} with high Ni content, the Al consumption by oxide introduced vacancy-type defects below the oxide. Such vacancy-type defects can promote oxygen incorporation by vacancy-assisted diffusion. Because grain boundaries are sinks for such defects and oxygen, oxygen diffusion via grain boundaries is also considered to be enhanced. Once oxygen penetrated and decollated grain boundaries, the grain growth was suppressed.

3.2 Annealing behaviors of vacancy-type defects in Ni_xAl_{1-x}

Figure 4 shows S values as a function of incident positron energy E for $Ni_xAl_{1-x}/SiO_2/Si$ [x = (a) 0.45, (b) 0.50, and (c) 0.55] before and after annealing. Annealing temperatures are shown in the figure. The mean implantation depth of positron is shown on the upper horizontal axis. The S values at $E \geq 10$ keV correspond to the annihilation of positrons in the SiO_2 layer and/or the Si substrate. The S values measured at $E \leq 10$ keV mainly correspond to the annihilation of positrons in the Ni_xAl_{1-x} layer. The solid curves for the samples are fitted to the experimental data, and the obtained depth distributions of S are shown in Fig. 5. The S values near the surface and the Ni_xA_{1-x}/SiO_2 interface are smaller than those in the central region of the Ni_xAl_{1-x} layer. Figure 6 shows the annealing behaviors of S measured at E = 2 keV for Ni_xAl_{1-x}. The mean implantation depth of positrons at this energy is about 15 nm. In the temperature range below 400°C, the S values for $Ni_{0.45}Al_{0.55}$ were higher than those for $Ni_{0.50}Al_{0.50}$ and $Ni_{0.55}Al_{0.45}$. After annealing at 800°C, the S values for the samples with different Ni contents

coincided.

Figure 7(a) shows the simulated *S* values for defect-free Al, Ni, and $Ni_{0.50}Al_{0.50}$ using QMAS (blue symbols). The simulated *S* value cannot be directly compared with the observed *S* values in Figs. 4–6 because the simulation did not involve the effect of background of measurements on *S*. A solid curve in Fig. 7(a) was obtained by the fitting assuming $S_{NiAl}(x) = S_{Ni}F(x) + S_{Al}[1 - F(x)]$ and $F(x) = a + bx + cx^2$, where *a*, *b*, and *c* are the constant. S_{Ni} and S_{Al} are the *S* values for defect-free Ni and Al, respectively. Doppler broadening spectra for well-annealed pure Ni and pure Al were measured, and their bulk *S* values were obtained to be 0.4024±0.0001 and 0.5265±0.0001, respectively. By using the bowing parameter obtained from the fitting of the simulated values, the *S* values corresponding to defect-free Ni_xAl_{1-x} (x = 0.45~0.55) were obtained to be 0.4431~0.4307. The *S* values for the Ni_xAl_{1-x} layers before and after annealing (Figs. 4 and 5) are larger than these values, suggesting the annihilation of positrons by vacancy-type defects.

The simulated *S* values for the annihilation of positrons trapped by Ni-vacancy (V_{Ni}), Al vacancy (V_{Al}), and their complexes [($V_{Ni}V_{Al}$, $(V_{Ni})_2$ and $(V_{Ni})_2V_{Al}$] in $Ni_{0.5}Al_{0.5}$ are shown in Fig. 7(a). An effect of oxygen coupling with vacancies on *S* is shown in Fig. 8(a). It can be seen that the *S* value for vacancy-oxygen complexes was smaller than that for 'intrinsic' vacancies. Figure 9 shows atomic configurations of (a) defect-free $Ni_{0.5}Al_{0.5}$, (c) V_{Ni}, and (e) V_{Ni} coupled with oxygen atoms (V_{Ni}-O) in $Ni_{0.5}Al_{0.5}$ on the supercell *ab*-plane. The horizontal (x) axis is parallel to [100], and the vertical axis (y) is parallel to [010]. Gray, light blue, and red circles correspond to Ni, Al, and oxygen, respectively. Projections of the positron densities corresponding to Fig. 9(a), (c), and (e) are shown in Fig. 9(b), (d), and (f), respectively, where the density decreases as "red > yellow > green > blue". As shown in Fig. 9(a) and (b), a positron mainly locates at interstitial sites in defect-free $Ni_{0.5}Al_{0.5}$ because of Coulomb repulsion from ion cores. When V_{Ni} is introduced into the supercell, the positron density is localized in V_{Ni} [Fig. 9(c) and (d)]. For V_{Ni}-O, the oxygen atom pushes away the neighboring Ni and locates inside of V_{Ni} [Fig. 9(e)]. This configuration increases the annihilation rate of positrons with high-momentum electrons of the oxygen atom [Fig. 9(f)] and is the major origin of the decrease in *S* for vacancy-oxygen complexes. Oxygen coupled with vacancy-type defects also decreases the lifetime of positrons trapped by such defects [Fig. 8(b)].

As shown in Fig. 6, the *S* values for $Ni_{0.45}Al_{0.55}$ were higher than those for $Ni_{0.50}Al_{0.50}$ and $Ni_{0.55}Al_{0.45}$. As discussed in the previous section, the oxygen incorporation was suppressed as Al content increased (Fig. 3). Thus, one major cause of the difference in *S* corresponding to the annihilation of positrons in the subsurface region can be attributed to the difference in the concentration of vacancy-oxygen complexes in Ni_xAl_{1-x}. The *S* values near the Ni_xAl_{1-x}/SiO_2 interface were lower

than those in the central regions of the layer (Fig. 5). The small value of *S* near the interface is also due to the annihilation of positrons trapped by complexes between vacancies and oxygen atoms diffused from the SiO_2 layer.

The lifetime spectra of positrons for Ni_xAl_{1-x} before and after annealing at 500°C were measured at $E = 4$ keV, where the mean implantation depth of positrons at this energy is 50 nm. The spectra were decomposed into three components. The derived lifetimes (τ_1, τ_2, and τ_3) and relative intensities (I_1, I_2, and I_3) are shown in Fig. 10. The values of τ_1 were almost constant before and after annealing and showed no dependence on Ni content. The values of τ_2 and τ_3 tended to increase as Ni content increased, and this tendency was enhanced by annealing.

The values of τ_3 suggest the formation of positronium (Ps: a hydrogen-like bound state between a positron and an electron, ref. 54) in Ni_xAl_{1-x}. Ps exhibits two spin states (singlet and triplet state), and they are called para-Ps (*p*-Ps) and ortho-Ps (*o*-Ps), respectively. The intrinsic lifetime of *p*-Ps is 0.125 ns, and that of *o*-Ps is 142 ns. The formation rate of *o*-Ps is three times of *p*-Ps. When *o*-Ps is formed in open spaces, a positron consisting of *o*-Ps may pick up an electron at the inner surface of the open space and annihilate with it (pick-off annihilation). Because the rate of the pick-off annihilation decreases as open spaces enlarge, one can estimate the average size of open spaces by measuring the *o*-Ps lifetime.

By using a semi-empirical model that assumes the formation of *o*-Ps in a spherical well [55] and the measured value of τ_3 (1.5–2.2 ns), the average diameter of open spaces was estimated to be about 0.5–0.6 nm. Thus, the third annihilation mode is likely due to the pick-off annihilation of *o*-Ps in open spaces or voids in Ni_xAl_{1-x}. Because the corresponding intensity of *o*-Ps (I_3) was almost constant before and after annealing [Fig. 10(b)], they are unlikely to be associated with grain boundaries. The value of τ_3 tended to increase as Ni content increased, and this tendency was enhanced by annealing. Thus, the open spaces detected by the third component can be associated with voids introduced by oxidation or oxygen incorporation into Ni_xAl_{1-x}.

The lifetime spectra of positrons for $Ni_{0.50}Al_{0.50}$ before and after annealing at 100–500°C were measured at $E = 4$ keV. Annealing behaviors of τ_i and I_i (i=1,2, and 3) are shown in Fig. 11(b) and (c). The variation of the *S* value measured at $E = 4$ keV is also shown in Fig. 11(a). No large change in the lifetime of the first annihilation mode (τ_1) was observed, where the average value of τ_1 was calculated to be 0.198 ns. In the three-component analysis, the annihilation mode of *p*-Ps is convoluted into the first annihilation mode, because of its short lifetime. Assuming that the lifetime of *p*-Ps and its intensity are 0.125 ns and $I_3/3$, respectively, the lifetime of positrons trapped by vacancy-type defects was estimated to be 0.202 ns. This lifetime is close to the simulated lifetime of positrons trapped by

monovacancies (V_{Ni}, V_{Al}), divacancies [$(V_{Ni})_2$, $V_{Ni}V_{Al}$], and trivacancy [$(V_{Ni})_2V_{Al}$] [Figs. 8(b)]. The vacancy-oxygen complexes such as $V_{Ni}V_{Al}$+O and $(V_{Ni})_2V_{Al}$+O are also candidate. The vacancy formation mechanism in NiAl has been studied from experimental and theoretical approaches [56–58]. In the thermal equilibrium state, the major point defects in NiAl are V_{Ni}s, Ni antisite defects, and their complexes because of a large difference between the formation energies of V_{Ni} and V_{Al}. In the present experiment, however, the state of Ni_xAl_{1-x} is far from the thermal equilibrium condition. A certain amount of V_{Al}s is expected to be introduced by oxygen incorporation and/or oxidation. Thus, the presence of V_{Al}s and related vacancy complexes cannot be excluded.

The values of τ_2 were almost constant in the measured temperature range, and their average value was calculated to be 0.460 ns [Fig. 11(b)]. This lifetime component is attributed to the annihilation of positrons trapped by vacancy clusters ($\geq V_{10}$) [30,37,59]. Thus, it can be concluded that vacancy-type defects with two different sizes coexist in Ni_xAl_{1-x}. The corresponding relative intensity (I_2) decreased as annealing temperature increased [Fig. 11(c)]. Although the concentration of vacancy clusters decreased as annealing temperature increased, vacancy-type defects with high concentrations remained after annealing at 400–500°C, which is the typical annealing temperature for the BEOL process. The observed decrease in the S value [Fig. 11(a)] can be attributed to not only the effect of the formation of vacancy-oxygen complex but also the annealing of vacancy clusters.

4. Summary

We used positron annihilation to study vacancy-type defects and their annealing behaviors in 100-nm-thick Ni_xAl_{1-x} (x = 0.45, 0.50, and 0.55) layers deposited on SiO_2/Si substrates. Crystalline structures and oxygen incorporation into the Ni_xAl_{1-x} layers were studied by using STEM, EDS, and APT. For $Ni_{0.45}Al_{0.55}$ after post-deposition annealing at 500°C, grains started to grow from the substrate. For the samples with higher Ni contents, however, the grain growth was suppressed. Upon annealing, oxygen diffused into the samples mainly through grain boundaries and was enhanced in the samples with high Ni contents. For Ni-rich Ni_xAl_{1-x}, the consumption of Al by oxidation promoted the diffusion of Ni to the bulk to compensate for the Al depletion. As a result, oxygen incorporation was enhanced via vacancy-assisted diffusion. The oxygen penetrating the grain boundary was considered to be a barrier to grain growth during annealing.

For as-deposited $Ni_{0.50}Al_{0.50}$, two different vacancy species coexisted: i) monovacancies and divacancy-type defects (including their oxygen complexes) and ii) vacancy clusters. The open volume of the vacancy clusters was estimated to be larger than V_{10}. No large change in the open spaces of the vacancy-type defects was observed in the annealing temperature below 500°C. The concentration of

vacancy clusters decreased as annealing temperature increased, but they were not fully annealed out below 800°C. The same is true for Ni_xAl_{1-x} with x = 0.45 and 0.55. The vacancy-type defects in the subsurface region and near the Ni_xAl_{1-x}/SiO_2 interface coupled with oxygen and form vacancy-oxygen complexes preferentially. The present work reported behaviors of vacancy-type defects and their interaction with incorporated oxygen, which are considered to closely relate to the resistivity of thin NiAl layers. Our results also demonstrate that a combination of positron annihilation and APT can provide useful information for advanced interconnects from the viewpoint of point defects.

Acknowledgements

A part of this work was supported by Japan Science and Technology Agency (JST) as part of Adopting Sustainable Partnerships for Innovative Research Ecosystem (ASPIRE), Grant Number JPMJAP2321. SI is grateful for the support from Tsukuba Materials Research. A part of this work was also supported by Advanced Research Infrastructure for Materials and Nanotechnology in Japan (ARIM) of the Ministry of Education, Culture, Sports, Science and Technology (MEXT), Proposal Number JPMXP1223AT5043. This work was supported by imec's industrial affiliate program on nano-interconnects. The authors would also like to thank Dr Alex Merkulov (imec) and Dr Richard J. H. Morris (imec) for their valuable input on the SIMS data analysis.

1. Tu, K. N. Recent advances on electromigration in very-large-scale-integration of interconnects. *J. Appl. Phys.* **2003**, 94, 5451–5473. DOI: 10.1063/1.1611263
2. Li, B.; Sullivan, T. D.; Lee, T. C.; Badami, D. Reliability challenges for copper interconnects. *Microelectronics Reliability* **2004**, 44, 365–380. DOI: 10.1016/j.microrel.2003.11.004
3. Tan, C. M.; Roy, A. Electromigration in ULSI interconnects. *Mater. Sci. Eng. R.* **2007**, 58, 1–75. DOI: 10.1016/j.mser.2007.04.002
4. Sondheimer, E. H. The mean free path of electrons in metals. *Advances Phys.* **1952**, 1, 1–42. DOI: 10.1080/00018735200101151
5. Mayadas, A. F.; Shatzkes, M. Electrical-resistivity model for polycrystalline films: the case of arbitrary reflection at external surfaces. *Phys. Rev. B* **1970**, 1, 1382–1389. DOI: 10.1103/PhysRevB.1.1382
6. De Clercq, M.; Moors, K.; Sankaran, K.; Pourtois, G.; Dutta, S.; Adelmann, C.; Magnus, W.; Sorée, B. Resistivity scaling model for metals with conduction band anisotropy. *Phys. Rev. Mat.* **2018**, 2, 033801. DOI: 10.1103/PhysRevMaterials.2.033801
7. Moors, K.; Sankaran, K.; Pourtois, G.; Adelmann, C. First-principles-based screening method for resistivity scaling of anisotropic metals. *Phys. Rev. Mat.* **2022**, 6, 123804. DOI: 10.1103/PhysRevMaterials.6.123804).
8. Gall, D. Electron mean free path in elemental metals. *J. Appl. Phys.* **2016**, 119, 085101. DOI: 10.1063/1.4942216.
9. Barmak, K.; Ezzat, S.; Gusley, R.; Jog, A.; Kerdsongpanya, S.; Khaniya, A.; Milosevic, E.; Richardson, W.; Sentosun, K.; Zangiabadi, A.; Gall, D.; Kaden, W. E; Mucciolo, E. R.; Schelling, P. K.; West, A. C.; Coffey, K. R. Epitaxial metals for interconnects beyond Cu. *J. Vac. Sci. Tech. A* **2020**, 38 033406. DOI: 10.1116/6.0000018
10. Gall, D. The search for the most conductive metal for narrow interconnect lines. *J. Appl. Phys.* **2020**, 127, 050901. DOI: 10.1063/1.5133671
11. Chen, L. H.; Kumar, S.; Yahagi, M.; Ando, D.; Sutou, Y.; Gall, D.; Sundararaman, R.; Koike, J. Interdiffusion reliability and resistivity scaling of intermetallic compounds as advanced interconnect materials. *J. Appl. Phys.* **2021**, 129, 035301. DOI: 10.1063/5.0026837
12. Van Troeye, B.; Sankaran, K.; Tőkei, Z.; Adelmann, C.; Pourtois, G. First-principles investigation of thickness-dependent electrical resistivity for low-dimensional interconnects. *Phys. Rev. B* **2023**, 108, 125117. DOI: 10.1103/PhysRevB.108.125117
13. Moon, J. H.; Jeong, E.; Kim, S.; Kim, T.; Oh, E.; Lee, K.; Han, H.; Kim, Y. K. Materials quest for advanced interconnect metallization in integrated circuits. *Adv. Sci.* **2023**, 10, 2207321. DOI: 10.1002/advs.202207321

14. Dutta, S.; Beyne, S.; Gupta, A.; Kundu, S.; Van Elshocht, S.; Bender, H.; Jamieson, G.; Vandervorst, W.; Bömmels, J.; Wilson, C. J.; Tőkei, Z.; Adelmann, C. Sub-100 nm^2 Cobalt Interconnects. *IEEE Electron Device Lett.* **2018**, 39, 731–734. DOI: 10.1109/LED.2018.2821923
15. Kelly, J.; Kamineni, V.; Lin, X.; Pacquette, A.; Hopstaken, M.; Liang, Y.; Amanapu, H.; Peethala, B.; Jiang, L.; Demarest, J.; Shobha, H.; Raymond, M.; Haran, B. Annealing and impurity effects in Co thin films for MOL contact and BEOL. *J. Electrochemical Soc.* **2019**, 166, D3100–D3109. DOI: 10.1149/2.0151901jes
16. Milosevic, E.; Kerdsongpanya, S.; McGahay, M. E.; Zangiabadi, A.; Barmak, K.; Gall, D. Resistivity scaling and electron surface scattering in epitaxial Co(0001) layers. *J. Appl. Phys.* **2019**, 125, 245105. DOI: 10.1063/1.5086458
17. Wen, L. G.; Roussel, P.; Pedreira, O. V.; Briggs, B.; Groven, B.; Dutta, S.; Popovici, M. I.; Heylen, N.; Ciofi, I.; Vanstreels, K.; Osterberg, F. W.; Hansen, O.; Petersen, D. H.; Opsomer, K.; Detavernie, C.; Wilson, C. J.; Elshocht, S. V.; Croes, K.; Bommels, J.; Tőkei, Z.; Adelmann, C. Atomic layer deposition of ruthenium with TiN interface for sub-10 nm advanced interconnects beyond copper. *ACS Appl. Materials Interfaces* **2016**, 8, 26119. DOI: 10.1021/acsami.6b07181
18. Dutta, S.; Sankaran, K.; Moors, K.; Pourtois, G.; Van Elshocht, S.; Bömmels, J.; Vandervorst, W.; Tőkei, Z.; Adelmann, C. Thickness dependence of the resistivity of platinum-group metal thin films, *J. Appl. Phys.* **2017**, 122, 025107. DOI: 10.1063/1.4992089
19. Milosevic, E.; Kerdsongpanya, S.; Zangiabadi, A.; Barmak, K.; Coffey, K. R.; Gall, D. Resistivity size effect in epitaxial Ru(0001) layers. *J. Appl. Phys.* **2018**, 124, 165105. DOI: 10.1063/1.5046430
20. Chen, L.; Ando, D.; Sutou, Y.; Gall, D.; Koike, J. NiAl as a potential material for liner- and barrier-free interconnect in ultrasmall technology node. *Appl. Phys. Lett.* **2018**, 113, 183503. DOI: 10.1063/1.5049620
21. Chen, L.; Ando, D.; Sutou, Y.; Yokogawa, S.; Koike, J. Liner- and barrier-free NiAl metallization: A perspective from TDDB reliability and interface status. *Appl. Surf. Sci.* **2019**, 497, 143810. DOI: 10.1016/j.apsusc.2019.143810
22. Soulié, J. P.; Tőkei, Z.; Swerts, J.; Adelmann, C. Thickness scaling of NiAl thin films for alternative interconnect metallization, *IEEE Int. Interconnect Tech. Conf. (IITC)* **2020**, 151–153. DOI: 10.1109/iitc47697.2020.9515638
23. Soulié, J. P.; Tőkei, Z.; Swerts, J.; Adelmann, C. Aluminide intermetallics for advanced interconnect metallization: thin film studies, *IEEE Int. Interconnect Tech. Conf. (IITC)* **2021**, S7-5. DOI: 10.1109/iitc51362.2021.9537441
24. Song, K. Y.; Na, S. J.; Choi, H.; Lee, H. J. Improvement of thermal stability of NiAl via employing Al capping layer for advanced interconnect applications. *Appl. Phys. Exp.* **2023**, 16, 035502. DOI:

10.35848/1882-0786/acbf01

25. Soulié, J. P.; Tőkei, Z.; Heylen, N.; Adelmann, C., Reduced resistivity of NiAl by backthinning for advanced interconnect metallization. *IEEE Int. Interconnect Tech. Conf. (IITC) & IEEE Mater. Advanced Metallization Conf. (MAM)* **2023**, 22–25. DOI: 10.1109/iitc/mam57687.2023.10154839
26. Yamaguchi, Y.; Kiewit, D. A.; Aoki, T.; Brittain, J. O. Electrical Resistivity of NiAl, CoAl, NiGa, and CoGaJ. *Appl. Phys.* **1968**, 39, 231–232. DOI: 10.1063/1.1655738
27. Jacobi, H.; Bassos, B.; Engell, H. J. Electrical properties of β-phase NiAl. *J. Phys. Chem. Solids* **1969**, 30, 1261–1271. DOI: 10.1016/0022-3697(69)90384-9
28. Butler, S. R.; Hanlon, J. E.; Wasilewski, R. Electric and magnetic properties of B2 structure compounds: NiAl, CoAl. *J. Phys. Chem. Solids* **1969**, 30, 1929–1934. DOI: 10.1016/0022-3697(69)90168-1
29. Miracle, D. B. The physical and mechanical properties of NiAl. *Acta Metall. Mater.* **1963***,* 41, 649–684. DOI: 10.1016/0956-7151(93)90001-9
30. Uedono, A.; Suzuki, T.; Nakamura, T.; Ohdaira, T.; Suzuki, R. Defects in electroplated Cu and their impact on stress migration reliability studied using monoenergetic positron beams. *Jpn. J. Appl. Phys.* **2007**, 46, 1938–1941. DOI: 10.1143/jjap.46.1938
31. Schultz, P. J.; Lynn, K. G. Interaction of positron beams with surfaces, thin films, and interfaces. *Rev. Mod. Phys.* **1988**, 60, 701–779. DOI: 10.1103/RevModPhys.60.701
32. Krause-Rehberg, R.; Leipner, H. S. *Positron Annihilation in Semiconductors, Solid-State Sciences* **1999***,* 127 (Springer-Verlag, Berlin) ISBN-10: 3540643710.
33. Uedono, A.; Suzuki, T.; Nakamura, T. Vacancy-type defects in electroplated Cu films probed by using a monoenergetic positron beam. *J. Appl. Phys.* **2004**, 95, 913–918. DOI: 10.1063/1.1635648
34. Maekawa, K.; Mori, K.; Suzumura, N.; Honda, K.; Hirose, Y.; Asai, K.; Uedono, A.; Kojima, M. *Microelectron. Eng.* **2008**, 85, 2137–2141. DOI: 10.1016/j.mee.2008.04.004
35. Yin, K. B.; Xia, Y. D.; Zhang, W. Q.; Wang, Q. J.; Zhao, X. N.; Li, A. D.; Liu, Z. G.; Hao Wei, L.; Chan, C. Y.; Cheung, K. L.; Bayes, M. W.; Yee, K. W. Room-temperature microstructural evolution of electroplated Cu studied by focused ion beam and positron annihilation lifetime spectroscopy. *J. Appl. Phys.* **2008**, 103, 066103. DOI: 10.1063/1.2874497
36. Onishi, T.; Mizuno, M.; Fujikawa, T.; Yoshikawa, T.; Munemasa, J.; Mizuno, M.; Kihara, T.; Araki, H.; Shirai, Y. A Study of difference in reflow characteristics between electroplated and sputtered Cu in a dual-damascene fabrication process for silicon semiconductor devices. *J. Elect. Mater.* **2011**, 40, 1384–1393. DOI: 10.1007/s11664-011-1521-4
37. Uedono, A.; Yamashita, Y.; Tsutsui, T.; Dordi, Y.; Li, S.; Oshima, N.; Suzuki, R. Vacancy clustering and its dissociation process in electroless deposited copper films studied by

monoenergetic positron beams. *J. Appl. Phys.* **2012**, 111, 104506. DOI: 10.1063/1.4719965

38. Uedono, A.; Nogami, T.; Gluschenkov, O.; Sulehria, Y.; Liu, J.; Tabata, T.; Lu, L.; Mitsuda, K.; Brown, I.; Okuno, Y. Impact of nanosecond laser annealing on vacancies in electroplated Cu films studied by monoenergetic positron beams. *J. Appl. Phys.* **2023**, 134, 135103. DOI: 10.1063/5.0166145
39. Van Veen, A.; Schut, H.; Clement, M.; de Nijs, J. M. M.; Kruseman, A.; IJpma, M. R. VEPFIT applied to depth profiling problems. *Appl. Sur. Sci.* **1995**, 85, 216–224. DOI: 10.1016/0169-4332(94)00334-3
40. O'Rourke, B. E.; Oshima, N.; Kinomura, A.; Suzuki, R. Development of a vertical slow positron beamline at AIST. *Jpn. J. App. Phys Conf. Proc.* **2014**, 2, 011304. DOI: 10.56646/jjapcp.2.0_011304
41. Kirkegaard, P.; Eldrup, M.; Mogensen, O. E.; Pedersen, N. J. Program system for analysing positron lifetime spectra and angular correlation curves. Comput. Phys. Commun. **1981**, 23, 307-335. DOI: 10.1016/0010-4655(81)90006-0
42. Ishibashi, S.; Tamura, T.; Tanaka, S.; Kohyama, M.; Terakura, K. Ab initiocalculations of electric-field-induced stress profiles for diamond/c−BN(110) superlattices. *Phys. Rev. B* **2007**, 76, 153310. DOI: 10.1103/PhysRevB.76.153310
43. Blöchl, P. E. Projector augmented-wave method. *Phys. Rev. B* **1994**, 50, 17953–17979. DOI: 10.1103/PhysRevB.50.17953
44. Perdew, J. P.; Burke, K.; Ernzerhof, M. Generalized Gradient Approximation Made Simple. *Phys. Rev. Lett.* **1996**, 77, 3865–3868. DOI: 10.1103/PhysRevLett.77.3865
45. Ishibashi, S. Computational study of positron–monovacancy interaction in d-block metals. *J. Phys. Soc. Jpn.* **2015**, 84, 083703. DOI:10.7566/JPSJ.84.083703
46. Ishibashi, S. Two-component density functional study of positron-vacancy interaction in metals and semiconductors. *Acta Physica Polonica* A **2017**, 132, 1602–1605. DOI: 10.12693/APhysPolA.132.1602
47. Boroński, E.; Nieminen, R. M. Electron-positron density-functional theory. *Phys. Rev. B* **1986**, 34, 3820–3831. DOI:10.1103/PhysRevB.34.3820
48. Puska, M. J.; Seitsonen, A. P.; Nieminen, R. M. *Phys. Rev. B* **1995**, 52, 10947–10961. DOI: 10.1103/PhysRevB.52.10947
49. Gault, B.; Chiaramonti, A.; Cojocaru-Mirédin, O.; Stender, P.; Dubosq, R.; Freysoldt, C.; Makineni, S. K.; Li, T.; Moody M.; Cairney, J. M. Atom probe tomography. *Nature reviews method primers*. **2021**, 1, 51. DOI: 10.1038/s43586-021-00047-w
50. Yang, J. C.; Schumann, E.; Levin, I.; Rühle, M. Transient oxidation of NiAl. *Acta Mater.* **1998**,

46, 2195–2201. DOI: 10.1016/S1359-6454(97)00378-9

51. Grabke, H. J. Oxidation of NiAl and FeAl. *Intermetallics* **1999**, 7, 1153–1158. DOI: 10.1016/S0966-9795(99)00037-0
52. Taylor, A.; Doyle, N. J. Further studies on the nickel-aluminum system. I. the β-NiAl and δ-Ni_2Al_3 phase fields. *J. Appl. Cryst.* **1972**, 5, 201–209. DOI: 10.1107/S0021889872009203
53. Brumm, M. W.; Grabke, H. J. Oxidation behavior of NiAl–II. cavity formation beneath the oxide scale on NiAl of different stoichiometries. *Corrosion Sci.* **1993**, 34, 547–561. DOI: 10.1002/chin.199324018
54. He, Y.; Luo, L.; Sushko, M. L.; Liu, C.: Baer, D. R.; Schreiber, D. K.; Rosso, K. M.; Wang, C. Vacancy ordering during selective oxidation of β-NiAl. *Materialia* **2020**, 12, 100783. DOI: 10.1016/j.mtla.2020.100783
55. Jean, Y. C. Positron annihilation spectroscopy for chemical analysis: a novel probe for microstructural analysis of polymers. *Microchem J.* **1990**, 42, 72–102. DOI: 10.1016/0026-265X(90)90027-3
56. Meyer, B.; Fähnle, M. Atomic defects in the ordered compound B2-NiAl: A combination of ab initio electron theory and statistical mechanics. *Phys. Rev. B* **1999**, 59, 6072–6082. DOI: 10.1103/PhysRevB.60.14492
57. Mishin, Y.; Farkas, D. Atomistic simulation of point defects and diffusion in B2 NiAl. *Scripta Materialia* **1998**, 39, 625–630. DOI: 10.1080/01418619708210290
58. Korzhavyi, P. A.; Ruban, A. V.; Lozovoi, A. Y.; Vekilov, Yu. Kh.; Abrikosov, I. A.; Johansson, B. *Phys. Rev. B* **2000**, 61, 6003–6018. DOI: 10.1103/PhysRevB.59.11693
59. Čížek, J.; Janeček, M.; Vlasák, T.; Smola, B.; Melikhova, O.; Islamgaliev, R. K.; Dobatkin S. V. The Development of Vacancies during Severe Plastic Deformation *Materials Transactions* **2019**, 60, 1533–1542. DOI: 10.2320/matertrans.MF201937

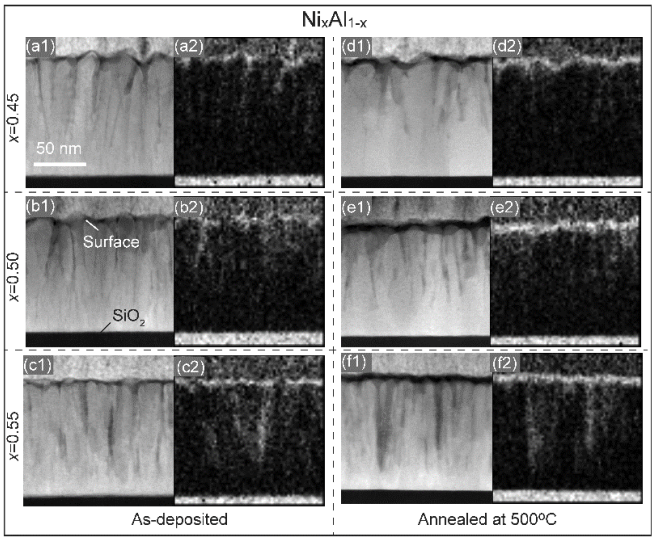

Fig. 1. Cross-sectional HAADF STEM images for Ni_xAl_{1-x} (x = 0.45, 0.50, and 0.55) before (a1, b1, and c1) and after annealing at 500°C (d1, e1, and f1). Values of x are shown on left side of figures. EDS maps for oxygen are also shown for Ni_xAl_{1-x} before [(a2), (b2), and (c2)] and after annealing [(d2), (e2), and (f2)].

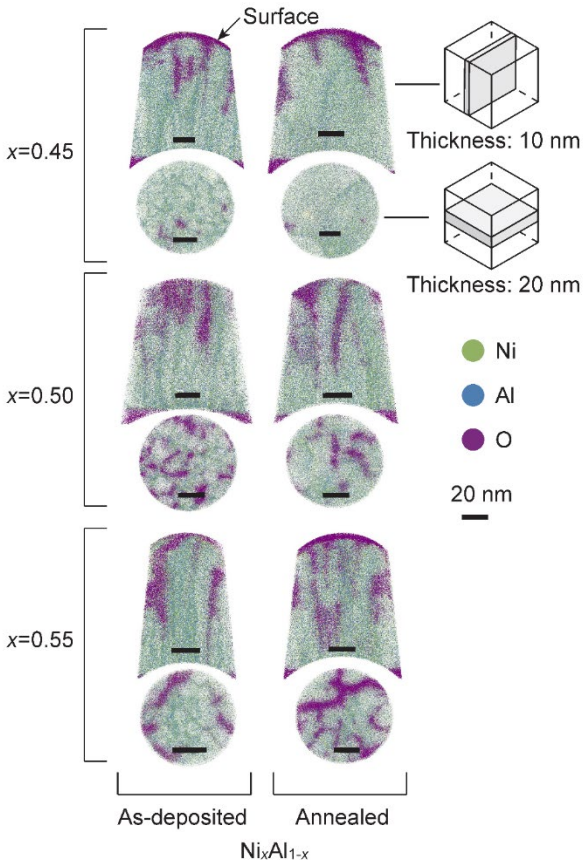

Fig. 2. Cross-sectional distributions of Ni, Al, and oxygen in Ni_xAl_{1-x} (x = 0.45, 0.50, and 0.55) before and after annealing at 500°C. Atom distributions were obtained from vertical and horizontal slices

from three-dimensional atom maps, respectively. Green, blue, and violet points correspond to Ni, Al, and oxygen, respectively.

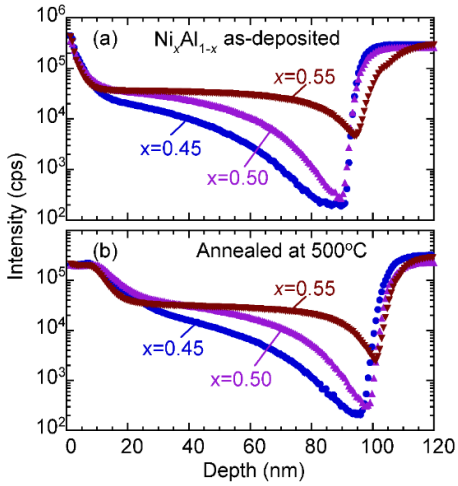

Fig. 3. Depth profiles of oxygen obtained from SIMS for Ni_xAl_{1-x} (x = 0.45, 0.50, and 0.55) before (a) and after annealing at 500°C (b).

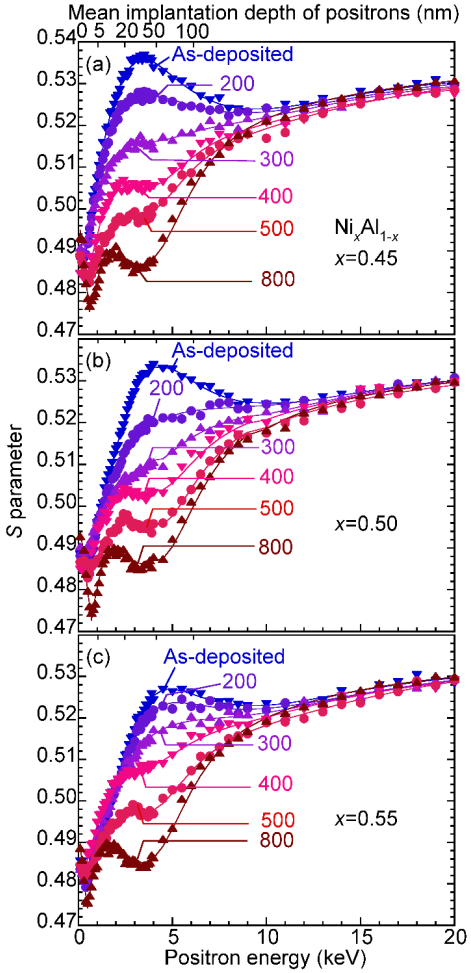

Fig. 4. S parameters as function of incident positron energy E for $Ni_xAl_{1-x}/SiO_2/Si$ [x = (a) 0.45, (b) 0.50, and (c) 0.55] before and after annealing. Annealing temperatures are shown in figures. Solid

curves are fitted to experimental data. Annealing temperatures are shown in figures.

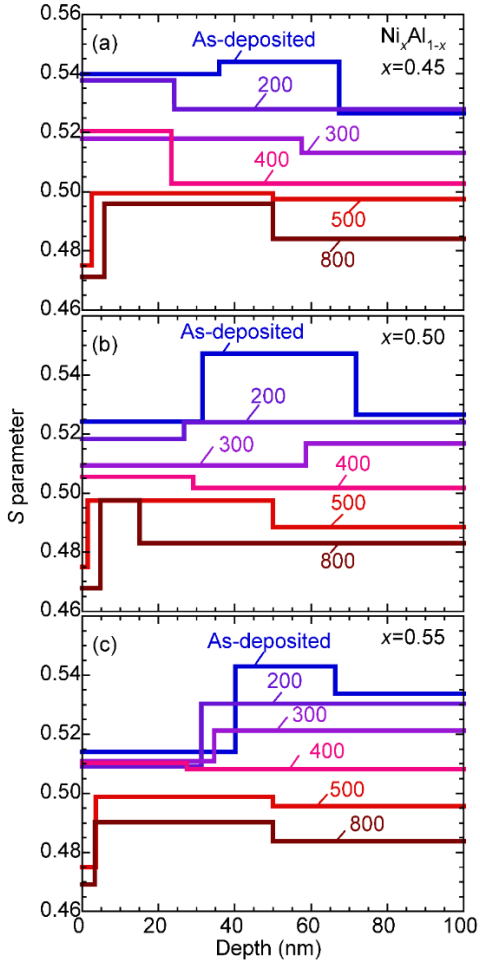

Fig. 5. Depth distributions of S for Ni_xAl_{1-x} [x = (a) 0.45, (b) 0.50, and (c) 0.55] before and after annealing.

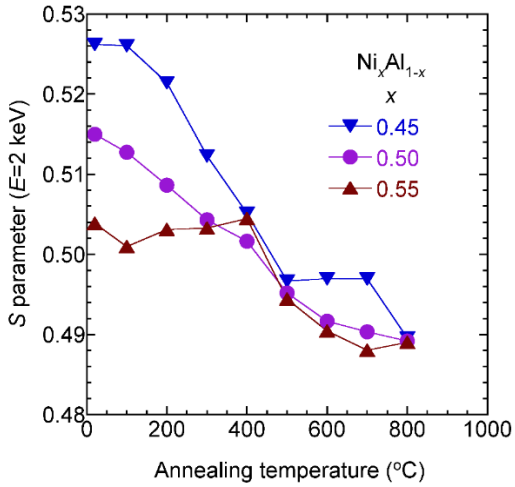

Fig. 6. Annealing behaviors of S measured at E = 2 keV for Ni_xAl_{1-x} (x = 0.45, 0.50, and 0.55).

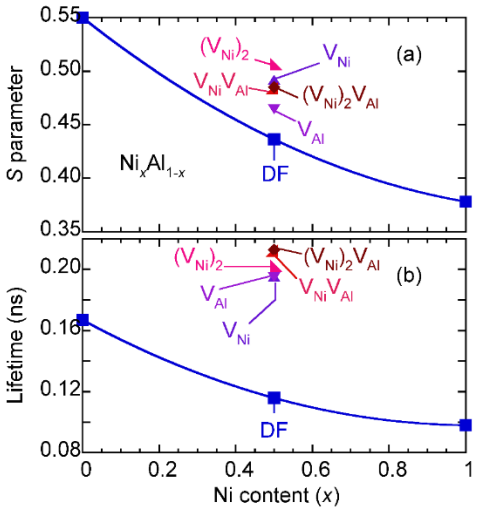

Fig. 7. Simulated (a) values of *S* and (b) positron lifetimes corresponding to annihilation of positrons from delocalized states in Ni, Al, and $Ni_{0.5}Al_{0.5}$ (defect-free: DF). Results for annihilation of positrons trapped by vacancy-type defects [V_{Ni}, V_{Al}, $V_{Ni}V_{Al}$, $(V_{NI})_2$, and $(V_{NI})_2Al$] in $Ni_{0.5}Al_{0.5}$ are also shown.

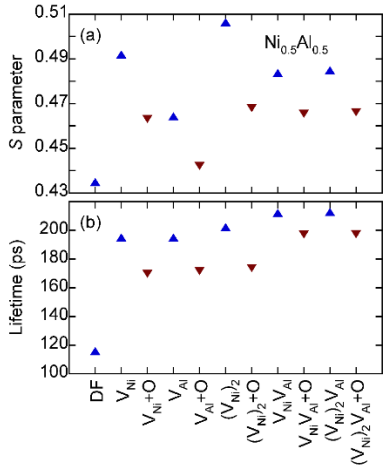

Fig. 8. Simulated (a) value of *S* and (b) positron lifetimes corresponding to annihilation of positrons trapped by vacancy-type defects and their complexes with oxygen atoms.

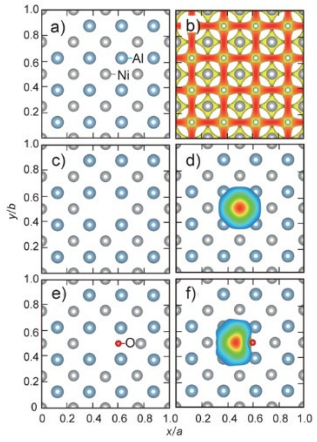

Fig. 9. Configurations of atoms for (a) defect-free $Ni_{0.5}Al_{0.5}$, (b) V_{Ni}, and (c) $V_{Ni}O$ in $Ni_{0.5}Al_{0.5}$.

Distributions of positron densities corresponding to (a), (b), and (c) are shown in (b), (d), and (f), respectively. Grey, light blue, and red circles correspond to Ni, Al, and oxygen, respectively.

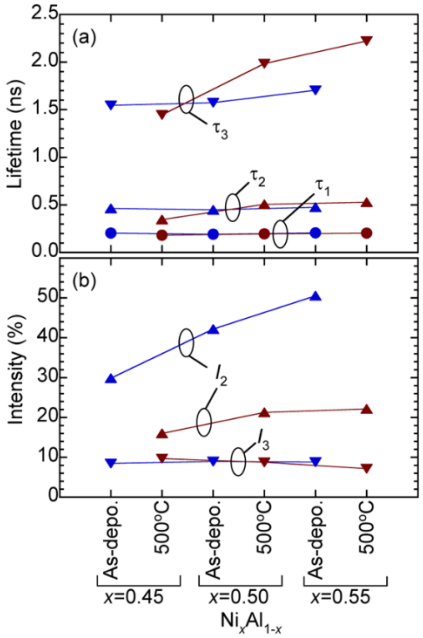

Fig. 10. Positron lifetimes (τ_i, i = 1, 2, and 3) and corresponding relative intensities (I_i) for Ni_xAl_{1-x} (x = 0.45, 0.50, and 0.55) before ("As-depo.") and after annealing at 500°C. Incident energy of positrons was fixed at E = 4 keV.

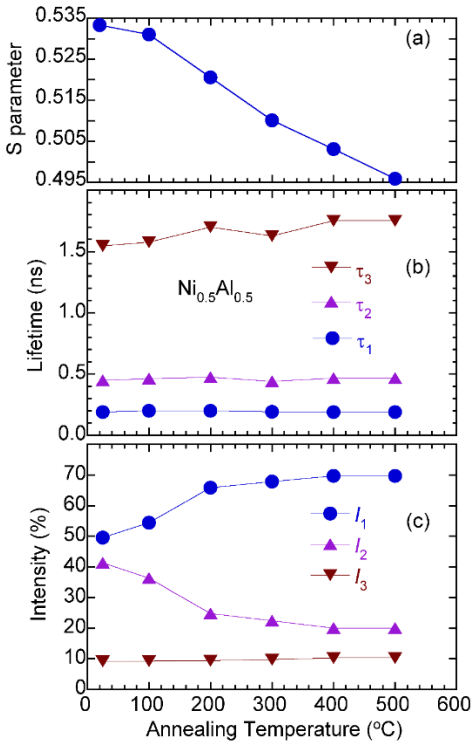

Fig. 11. Annealing behaviors of (a) values of S, (b) positron lifetimes, and (c) corresponding relative intensities for $Ni_{0.5}A_{0.5}$. Incident energy of positrons was fixed at E = 4 keV.